**53rd AIAA/ASME/ASCE/AHS/ASC Structures, Structural Dynamics and Materials Conference
20th AI**
23 - 26 April 2012, Honolulu, Hawaii

AIAA 2012-1713

Strain-Based Analysis for Geometrically Nonlinear Beams: A Modal Approach

Weihua Su[1] and Carlos E. S. Cesnik[2]
University of Michigan, Ann Arbor, MI, 48109-2140

A strain-based geometrically nonlinear beam formulation for structural dynamic and aeroelastic analysis of slender beams and wings has been successfully applied to study the coupled nonlinear aeroelasticity and flight dynamics of different very flexible aircraft. As an extension to the solution technique based on the nonlinear finite element developed by the authors, a modal-based approach is discussed in this paper to solve the strain-based nonlinear beam equations. The modal approach is applied to study geometrically nonlinear static and transient problems of constrained and free slender beams, subject to external structural or aero-dynamic excitations. The efficiency of the modal solution is also compared to that of the finite-element approach.

Nomenclature

a_0 = local aerodynamic frame, with a_{0y} axis aligned with zero lift line of airfoil
a_1 = local aerodynamic frame, with a_{1y} axis aligned with airfoil motion velocity
B = body reference frame
B^F, B^M = influence matrices for the distributed forces and moments
b = positions and orientations of the B frame, as time integral of β
b_c = semichord of airfoil, m
C_{FF}, C_{FB}, C_{BF}, C_{BB}
  = components of the generalized damping matrix
$\bar{C}_{FF}$, $\bar{C}_{FB}$, $\bar{C}_{BF}$, $\bar{C}_{BB}$
  = components of the generalized damping matrix in modal equations
C^{Ba_1} = rotation matrix from the a_1 frame to the B frame
C^{GB} = rotation matrix from B frame to G frame
c = chord length, m
d = distance of midchord in front of beam reference axis, m
F_1, F_2, F_3
  = influence matrices in inflow equations with independent variables
$\bar{F}_{1F}$, $\bar{F}_{2F}$ = flexible components of influence matrices F_1 and F_2 in the modal equations
F^{aero}, M^{aero}
  = nodal aerodynamic forces and moments
F^{dist}, F^{pt} = distributed and point forces
G = global (inertial) reference frame
g = gravity acceleration column vector, m/s^2
H_{hb} = matrix consisting of influence from the Jacobian J_{hb} and body angular velocities ω_B
h = absolute positions and rotations of beam nodes
J = Jacobian matrix
K_{FF} = components of the generalized stiffness matrix
$\bar{K}_{FF}$ = components of the generalized stiffness matrix in modal equations
L = beam/wing span, m

---

[1] Post-doctoral Research Fellow (suw@umich.edu), Department of Aerospace Engineering, Senior Member AIAA.
[2] Professor (cesnik@umich.edu), Department of Aerospace Engineering, Fellow AIAA.

l_{mc}, m_{mc}, d_{mc}
  = aerodynamic loads on an airfoil about its midchord
l_{ra}, m_{ra}, d_{ra}
  = aerodynamic loads on an airfoil about beam reference axis
m = mass per span, kg/m
M, C, K = discrete mass, damping, and stiffness matrices of whole system
$M_{FF}, M_{FB}, M_{BF}, M_{BB}$
  = components of generalized mass matrix
$\bar{M}_{FF}, \bar{M}_{FB}, \bar{M}_{BF}, \bar{M}_{BB}$
  = components of generalized mass matrix in modal equations
M^{dist}, M^{pt} = distributed and point moments
N = influence matrix for gravity force
P_B = inertia position of B frame, resolved in G frame
p_B, θ_B = position and orientation of B frame, as time integral of v_B and ω_B, respectively
p_w = position of w frame with respect to B frame
R_B, R_F = rigid-body and flexible components of generalized load vector
$\bar{R}_B, \bar{R}_F$ = rigid-body and flexible components of generalized load vector in modal equations
s = beam curvilinear coordinate, m
t = time, s
v_B, ω_B = linear and angular velocities of B frame, resolved in B frame itself
W^{ext}, W^{int} = external and internal virtual work, respectively
w = local beam reference frame defined at each node along beam reference line
$\dot{y}, \dot{z}$ = airfoil translational velocity components resolved in a_0 frame, m/s
$\dot{\alpha}$ = airfoil angular velocity about a_{0x} axis, rad/s
β = body velocities, with translational and angular components, resolved in B frame
ε = total elastic strain vector of aircraft
ε_e = element elastic strain vector
ε^0 = initial (prescribed) elastic strain vector
ζ = quaternions defining orientation of B frame
η = modal coordinates
θ = rotations of beam nodes, rad
λ = inflow states, m/s
λ_0 = inflow velocities, m/s
ρ = air density, kg/m^3
Φ = (strain) normal mode shape
Φ_C, Φ_F, Φ_B
  = complete, flexible (strain), and rigid-body components of the strain-based modeshape, respectively
$\Omega_\zeta(\beta)$ = coefficient matrix of quaternion equations, a function of body angular velocities

Abbreviation
$c.g.$ = center of gravity
$l.e.$ = leading edge

Subscript
B = reference to B frame
BB, BF = components of a matrix with respect to body/flexible differential equations of motion
F = reference to flexible degrees of freedom
FB, FF = components of a matrix with respect to flexible/body differential equations of motion
hb = h vector with respect to motion of B frame
$h\varepsilon$ = h vector with respect to strain ε
pb = nodal position with respect to motion of B frame
$p\varepsilon$ = nodal position with respect to strain ε
θb = nodal rotation with respect to motion of B frame
$\theta\varepsilon$ = nodal rotation with respect to strain ε

2
American Institute of Aeronautics and Astronautics

I.   Introduction

IN studies of helicopters and very flexible aircraft (e.g., glider and high-altitude long-endurance aircraft), the slender blades and wings of these vehicles can be modeled as beams by taking advantage of the structure slenderness. However, the high flexibility associated with the blades and wings brings some special requirements to the beam formulation applied to the analysis. From the previous investigations,[1] the slender wings of very flexible aircraft may undergo large deformations under normal operating loads, exhibiting geometrically nonlinear behaviors. The structural dynamic and aeroelastic behavior of the aircraft may change significantly due to those large deflections of these flexible wings. In addition, very flexible aircraft usually see the coupling between the low-frequency elastic modes of their slender wings and the rigid-body motion of the complete aircraft.[1-5] Therefore, the coupled effects between the large deflection due to the wing flexibility and the aeroelastic/flight dynamic characteristics of the complete aircraft must be properly accounted for in a nonlinear aeroelastic solution. For this purpose, a beam formulation that is able to capture the geometrically nonlinear wing deformation is required to serve as the basis of the nonlinear structural dynamic and aeroelastic analysis of very flexible aircraft.

There have been different geometrically nonlinear formulations established for slender beams. One may classify the formulations based on the solution methodology, namely the displacement-based formulation (e.g., Ref. 6), the mixed-form formulation (e.g., Ref. 7-9), and the strain (or stress)-based formulation (e.g., Refs. 10, 11). Their difference lies in the definition of independent variables to represent the displacement field and the treatment of the beam reference line's rotation in the solution. A brief description of the three types of beam formulations was provided by Su and Cesnik,[12] while a comprehensive discussion on the three types of formulations for the structural, aeroelastic, and flight dynamic analysis of very flexible aircraft was done by Palacios et al.[13] They compared the solutions in terms of their numerical efficiency and simplicity for integrated flight dynamic analysis with full aircraft flexibility.

A complete treatment of the strain-based geometrically nonlinear beam formulation was introduced by the Su and Cesnik.[12] The strain-based formulation defines the extensional strain, bending and twist curvatures of the beam reference line as the independent degrees of freedom, while transverse shears are not explicitly included in them. Unlike the strain-based formulations presented in the literature (e.g., Ref. 10), which enforce the beam equilibrium equation and strain-displacement kinematics simultaneously with Lagrange multipliers, the formulation introduced in Ref. 12 solves these equations iteratively. Thus, the derived governing equation is the classic form of second-order differential equation, which simplifies the solution process. For that, the force and displacement boundary conditions are considered in a different way than Ref. 10. These improvements in this formulation make it more flexible in modeling arbitrary beam configurations under different loading conditions. Besides the above-mentioned advantages, the strain-based formulation brings additional benefits to control studies, since the curvatures are the variables that can be directly measured by the strain sensors. This formulation may also demonstrate great computational efficiency, due to the reduction in degrees of freedom for the same complex deformation when compared to the displacement-based or the mixed-form formulations. Lastly, the strain-based formulation is efficient in solving geometrically nonlinear static problems, as it features a constant stiffness matrix (for statically determinate beams). This advantage, however, does not hold in nonlinear transient solutions, where the inertia and damping of the system need to be updated according to the instantaneous beam deformation states.

Different solution techniques have been applied to solve the developed geometrically nonlinear beam formulation. A common approach is to use the well-developed finite-element method. Numerous applications of finite-element method can be found in literature. The strain-based beam formulation introduced in Ref. 12 was also solved by using this approach. Generally, finite-element solutions may converge to the exact solution as the mesh is refined. However, the dimension of the problem may dramatically increase with the refinement of mesh, which brings higher computational cost for the solution. Since a fast solution is always desired in the nonlinear structural dynamic and aeroelastic analysis of very flexible aircraft, other solution techniques have also been developed and applied in studies.

In addition to the finite-element method, modal approach is another popular technique that is widely used in engineering analysis. One of its important advantages is its significant reduction in the dimension of the problem. Moreover, normal modes in the modal analysis may de-couple the system matrices and further simplify the problem. One may also find significant characteristics of the vibrational behaviors by using modal approaches. Because of the advantages of the modal approaches, it has been applied in various studies to solve the beam dynamics and aeroelasticity of very flexible wings and aircraft. Tang and Dowell[14-16] performed both experimental and numerical studies on the nonlinear flutter boundary, gust response, and limit-cycle oscillations of a slender cantilever beam. In their analytical study, general mode shape functions were applied to solve the nonlinear beam equations in terms of generalized coordinates. Patil and Althoff[17] presented a Galerkin approach for the solution of the nonlinear beam

equations. In this study, the mixed-form intrinsic geometrically nonlinear beam equations of motion including the kinematic equations and boundary conditions (Ref. 9) were weighted by appropriate function to represent the rate of change of internal energies and the work done by external forces. In their numeric analysis about a slender beam, they demonstrated the advantage of the Galerkin method over the finite-element method in terms of the convergence speed and accuracy. Palacios[18] applied nonlinear normal modes method to solve the mixed-form intrinsic nonlinear beam equations. The nonlinear modal equations in intrinsic coordinates were obtained from integrals involving only products of the modeshapes and known sectional properties. The nonlinear normal modes were sought through an asymptotic approximation to the invariant manifolds that define them in the space of intrinsic modal coordinates. Dynamics of isotropic and anisotropic beams were solved with this method.

The strain-based nonlinear beam formulation[12] has been employed by the authors and their co-workers for solving aeroelastic problems.[3-5, 19, 20] Common in these applications, the beam formulation was solved in a finite-element approach. In this paper, a modal solution of the strain-based beam formulation is discussed, where the number of degrees of freedom is further reduced by using the linear normal modes. As the beam dynamics derived in Ref. 12 are represent by the strain (curvature) and its time derivatives, the normal modes used in this paper will be strain modes. The numerical study demonstrates the accuracy and efficiency of the modal solution approach.

II.   Theoretical Formulation

The finite-element solution of the strain-based geometrically nonlinear beam formulation has been discussed by Su and Cesnik.[12] A introduction of the derivation of the finite-element equations of motion with the modal transformation is presented here for completeness.

A. System Frames

As shown in Fig. 1a, a fixed global (inertial) frame G is firstly defined. A body frame $B(t)$ is then built in the global frame to describe the vehicle position and orientation, with $B_x(t)$ pointing to the right wing, $B_y(t)$ pointing forward, and $B_z(t)$ being cross product of $B_x(t)$ and $B_y(t)$. The position and orientation b and the time derivatives $\dot{b}$ and $\ddot{b}$ of the B frame can be defined as

$$b = \begin{Bmatrix} p_B \\ \theta_B \end{Bmatrix} \qquad \dot{b} = \beta = \begin{Bmatrix} \dot{p}_B \\ \dot{\theta}_B \end{Bmatrix} = \begin{Bmatrix} v_B \\ \omega_B \end{Bmatrix} \qquad \ddot{b} = \dot{\beta} = \begin{Bmatrix} \ddot{p}_B \\ \ddot{\theta}_B \end{Bmatrix} = \begin{Bmatrix} \dot{v}_B \\ \dot{\omega}_B \end{Bmatrix} \tag{1}$$

where p_B and θ_B are body position and orientation, both resolved in the body frame B. Note that the origin of the body frame is arbitrary in the vehicle and it does not have to be the location of the vehicle's center of gravity.

Within the body frame, a local beam frame w is built at each node along the beam reference line (Fig. 1b), which is used to define the nodal position and orientation. Vectors $w_x(s,t)$, $w_y(s,t)$, and $w_z(s,t)$ are bases of the beam frame, whose directions are pointing along the beam reference axis, toward the leading edge (front), and normal to the beam surface, respectively, resolved in the body frame. s is the curvilinear beam coordinate.
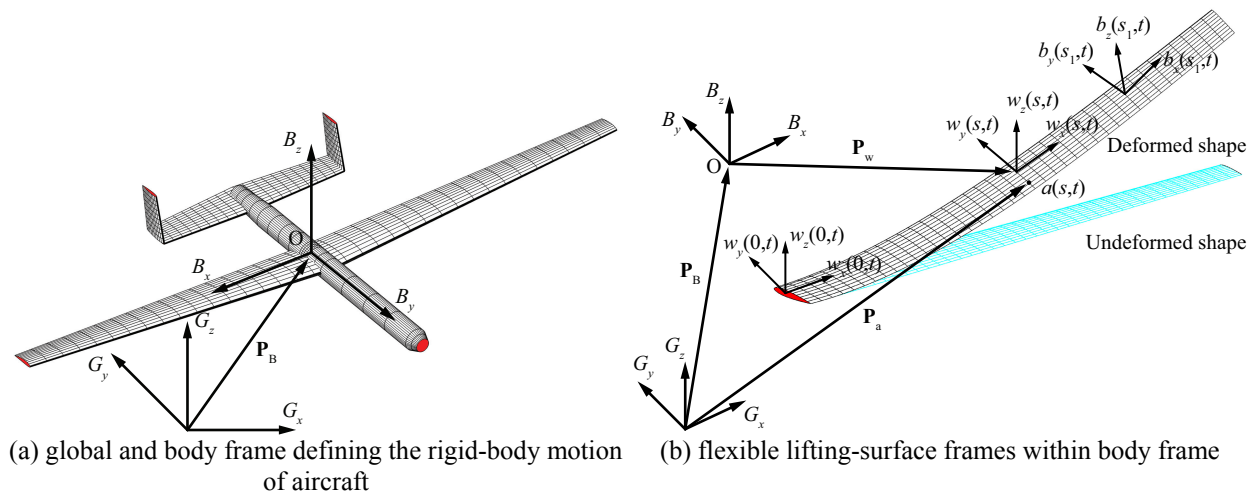

(a) global and body frame defining the rigid-body motion of aircraft

(b) flexible lifting-surface frames within body frame

Figure 1. Basic beam reference frames.

4

American Institute of Aeronautics and Astronautics

B. Elements with Constant Strains

A nonlinear beam element[12] is used to model the elastic deformation of slender beams. Strains of the beam reference line are considered as the independent variables in the solution. The strain-based formulation allows simple shape functions for the element. Constant-value functions are used here. Thus, the strain vector of an element is denoted as

$$\varepsilon_e^T = \left\{ \varepsilon_x \quad \kappa_x \quad \kappa_y \quad \kappa_z \right\} \tag{2}$$

where ε_x is the extensional strain, κ_x, κ_y, and κ_z are the twist of the beam reference line, bending about the local w_y axis, and bending about the local w_z axis, respectively. The total strain vector of the complete aircraft is obtained by assembling the global strain vector:

$$\varepsilon^T = \left\{ \varepsilon_{e1}^T \quad \varepsilon_{e2}^T \quad \varepsilon_{e3}^T \quad \ldots \right\} \tag{3}$$

Transverse shear strains are not explicitly included in this equation. However, shear strain effects are included in the constitutive relation.[21] Complex geometrically nonlinear deformations can be represented by such a constant strain distribution over each element. To represent the quadratic nodal displacement field that will be recovered from the constant strain, the element is defined with three equally spaced nodes. Some of the functions, such as inertia and distributed load, are assumed to vary linearly between the three nodes of each element. The values of these functions over the element can be obtained from its nodal values using linear Lagrange interpolation functions.

C. Nodal Displacement and Jacobians

The position and orientation of each node along the beam are defined by a vector consisting of 12 components, denoted as

$$h(s)^T = \left\{ \left[p_B + p_w(s) \right]^T \quad w_x(s)^T \quad w_y(s)^T \quad w_z(s)^T \right\} \tag{4}$$

where p_w is the position of the w frame resolved in the body frame. The derivatives and variations of the dependent variable h are related with those of the independent ones as

$$\delta h = J_{h\varepsilon}\delta\varepsilon + J_{hb}\delta b \qquad \dot{h} = J_{h\varepsilon}\dot{\varepsilon} + J_{hb}\dot{b} = J_{h\varepsilon}\dot{\varepsilon} + J_{hb}\beta$$
$$dh = J_{h\varepsilon}d\varepsilon + J_{hb}db \qquad \ddot{h} = J_{h\varepsilon}\ddot{\varepsilon} + \dot{J}_{h\varepsilon}\dot{\varepsilon} + J_{hb}\dot{\beta} + \dot{J}_{hb}\beta \tag{5}$$

where

$$J_{h\varepsilon} \equiv \frac{\partial h}{\partial \varepsilon} \qquad J_{hb} \equiv \frac{\partial h}{\partial b} \tag{6}$$

are the transformation Jacobians obtained from the beam kinematics. The other necessary Jacobian matrices, including $J_{p\varepsilon}$, $J_{\theta\varepsilon}$, J_{pb}, and $J_{\theta b}$, which relate the nodal positions and rotations to the independent variables, can be derived from $J_{h\varepsilon}$ and J_{hb}.[3, 12]

D. Finite-Element Equations of Motion

The equations of motion of the system are derived by following the principle of virtual work. The total virtual work done on a beam is found by integrating the products of all internal and external forces and the corresponding virtual displacements over the volume, which is given as

$$\delta W = \int_V \delta u^T(x,y,z) f(x,y,z) dV \tag{7}$$

5

American Institute of Aeronautics and Astronautics

where f represents general forces acting on a differential volume. This may include internal elastic forces, inertial forces, gravity forces, external distributed forces and moments, external point forces and moments, etc. δu is the corresponding virtual displacement. When beam cross-sectional properties are known, the integration of Eq. (7) over the beam volume is simplified to the integration along the beam coordinate s. This integration is first numerically performed over each beam element, followed by the assemblage of the element quantities to obtain the total virtual work on the whole beam. This paper gives a brief overview of the equations of motion, while the detailed derivation process can be found in Refs. 4, 12. The virtual work due to internal and external loads are given by

$$\delta W^{int} = -\delta h^T M \ddot{h} - \delta h^T M H_{hb} \beta - \delta h^T M \dot{J}_{hb} \beta - \delta \varepsilon^T C \dot{\varepsilon} - \delta \varepsilon^T K \left(\varepsilon - \varepsilon^0 \right)$$

$$\delta W^{ext} = -\delta h^T N g + \delta p_w^T B^F F^{dist} + \delta \theta^T B^M M^{dist} + \delta p_w^T F^{pt} + \delta \theta^T M^{pt}$$

(8)

The dependent variables (h, p_w, and θ) can be replaced by the independent variable by applying the Jacobians [see Eq. (6)] and their subsets. Therefore, the total virtual work on a beam can be written as

$$\delta W = \delta W^{int} + \delta W^{ext}$$

$$= -\left\{ \delta \varepsilon^T \quad \delta b^T \right\} \left(\begin{bmatrix} J_{h\varepsilon}^T M J_{h\varepsilon} & J_{h\varepsilon}^T M J_{hb} \\ J_{hb}^T M J_{h\varepsilon} & J_{hb}^T M J_{hb} \end{bmatrix} \begin{Bmatrix} \ddot{\varepsilon} \\ \dot{\beta} \end{Bmatrix} + \begin{bmatrix} J_{h\varepsilon}^T M \dot{J}_{h\varepsilon} & 0 \\ J_{hb}^T M \dot{J}_{h\varepsilon} & 0 \end{bmatrix} \begin{Bmatrix} \dot{\varepsilon} \\ \beta \end{Bmatrix} + \begin{bmatrix} 0 & J_{h\varepsilon}^T M H_{hb} \\ 0 & J_{hb}^T M H_{hb} \end{bmatrix} \begin{Bmatrix} \dot{\varepsilon} \\ \beta \end{Bmatrix} \right.$$

$$\left. + \begin{bmatrix} 0 & 2 J_{h\varepsilon}^T M \dot{J}_{hb} \\ 0 & 2 J_{hb}^T M \dot{J}_{hb} \end{bmatrix} \begin{Bmatrix} \dot{\varepsilon} \\ \beta \end{Bmatrix} + \begin{bmatrix} C & 0 \\ 0 & 0 \end{bmatrix} \begin{Bmatrix} \dot{\varepsilon} \\ \beta \end{Bmatrix} + \begin{bmatrix} K & 0 \\ 0 & 0 \end{bmatrix} \begin{Bmatrix} \varepsilon \\ b \end{Bmatrix} - \begin{Bmatrix} K \varepsilon^0 \\ 0 \end{Bmatrix} \right)$$

$$+ \left\{ \delta \varepsilon^T \quad \delta b^T \right\} \left(-\begin{bmatrix} J_{h\varepsilon}^T \\ J_{hb}^T \end{bmatrix} N g + \begin{bmatrix} J_{p\varepsilon}^T \\ J_{pb}^T \end{bmatrix} B^F F^{dist} + \begin{bmatrix} J_{\theta\varepsilon}^T \\ J_{\theta b}^T \end{bmatrix} B^M M^{dist} + \begin{bmatrix} J_{p\varepsilon}^T \\ J_{pb}^T \end{bmatrix} F^{pt} + \begin{bmatrix} J_{\theta\varepsilon}^T \\ J_{\theta b}^T \end{bmatrix} M^{pt} \right)$$

(9)

Following the same process described in Ref. 4, the elastic equations of motion are eventually derived as

$$\begin{bmatrix} M_{FF} & M_{FB} \\ M_{BF} & M_{BB} \end{bmatrix} \begin{Bmatrix} \ddot{\varepsilon} \\ \dot{\beta} \end{Bmatrix} + \begin{bmatrix} C_{FF} & C_{FB} \\ C_{BF} & C_{BB} \end{bmatrix} \begin{Bmatrix} \dot{\varepsilon} \\ \beta \end{Bmatrix} + \begin{bmatrix} K_{FF} & 0 \\ 0 & 0 \end{bmatrix} \begin{Bmatrix} \varepsilon \\ b \end{Bmatrix} = \begin{Bmatrix} R_F \\ R_B \end{Bmatrix}$$

(10)

where the generalized inertia, damping, and stiffness matrices are

$$M_{FF}(\varepsilon) = J_{h\varepsilon}^T M J_{h\varepsilon} \qquad M_{FB}(\varepsilon) = J_{h\varepsilon}^T M J_{hb}$$

$$M_{BF}(\varepsilon) = J_{hb}^T M J_{h\varepsilon} \qquad M_{BB}(\varepsilon) = J_{hb}^T M J_{hb}$$

$$C_{FF}(\varepsilon, \dot{\varepsilon}, \beta) = C + J_{h\varepsilon}^T M \dot{J}_{h\varepsilon} \qquad C_{FB}(\varepsilon, \dot{\varepsilon}, \beta) = J_{h\varepsilon}^T M H_{hb} + 2 J_{h\varepsilon}^T M \dot{J}_{hb}$$

$$C_{BF}(\varepsilon, \dot{\varepsilon}, \beta) = J_{hb}^T M \dot{J}_{h\varepsilon} \qquad C_{BB}(\varepsilon, \dot{\varepsilon}, \beta) = J_{hb}^T M H_{hb} + 2 J_{hb}^T M \dot{J}_{hb}$$

$$K_{FF} = K$$

(11)

and the generalized force vector is

$$\begin{Bmatrix} R_F \\ R_B \end{Bmatrix} = \begin{Bmatrix} K_{FF} \varepsilon^0 \\ 0 \end{Bmatrix} - \begin{bmatrix} J_{h\varepsilon}^T \\ J_{hb}^T \end{bmatrix} N g + \begin{bmatrix} J_{p\varepsilon}^T \\ J_{pb}^T \end{bmatrix} B^F F^{dist} + \begin{bmatrix} J_{\theta\varepsilon}^T \\ J_{\theta b}^T \end{bmatrix} B^M M^{dist} + \begin{bmatrix} J_{p\varepsilon}^T \\ J_{pb}^T \end{bmatrix} F^{pt} + \begin{bmatrix} J_{\theta\varepsilon}^T \\ J_{\theta b}^T \end{bmatrix} M^{pt}$$

(12)

where N, B^F, and B^M are the influence matrices for the gravity force, distributed forces, and distributed moments, respectively, which come from the numerical integration. The generalized force vector involves the effects from initial strains ε^0, gravity fields g, distributed forces F^{dist}, distributed moments M^{dist}, point forces F^{pt}, point moments M^{pt}. The aerodynamic forces and moments are considered as distributed loads.

E. Unsteady Aerodynamics

The distributed loads F^{dist} and M^{dist} in Eq. (12) are divided into aerodynamic loads and user-supplied loads. The unsteady aerodynamic loads used in the current study are based on the two dimensional (2-D) finite-state inflow theory provided in Ref. 22. The theory calculates aerodynamic loads on a thin airfoil section undergoing large motions in an incompressible inviscid subsonic flow. The lift, moment, and drag of a thin 2-D airfoil section about its midchord are given by

$$l_{mc} = \pi \rho_\infty b_c^2 \left(-\ddot{z} + \dot{y}\dot{\alpha} - d\ddot{\alpha} \right) + 2\pi \rho_\infty b_c \dot{y}^2 \left[-\frac{\dot{z}}{\dot{y}} + \left(\frac{1}{2} b_c - d \right) \frac{\dot{\alpha}}{\dot{y}} - \frac{\lambda_0}{\dot{y}} \right]$$

$$m_{mc} = \pi \rho_\infty b_c^2 \left(-\frac{1}{8} b_c^2 \ddot{\alpha} - \dot{y}\dot{z} - d\dot{y}\dot{\alpha} - \dot{y}\lambda_0 \right) \tag{13}$$

$$d_{mc} = -2\pi \rho_\infty b_c \left(\dot{z}^2 + d^2 \dot{\alpha}^2 + \lambda_0^2 + 2d\dot{z}\dot{\alpha} + 2\dot{z}\lambda_0 + 2d\dot{\alpha}\lambda_0 \right)$$

where b_c is the semichord and d is the distance of the midchord in front of the reference axis. The quantity $-\dot{z}/\dot{y}$ is the angle of attack that consists of the contribution from both the pitching angle and the unsteady plunging motion of the airfoil. The different velocity components are shown in Fig. 2. The coefficients c_i through g_i are based upon the geometry of trailing-edge flaps and their expressions are given in Ref. 22.
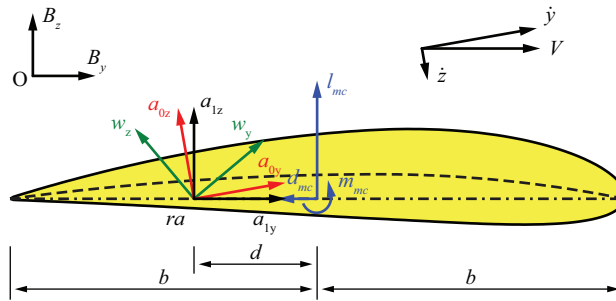
Figure 2. Airfoil coordinate systems and velocity components.

The inflow parameter λ_0 accounts for induced flow due to free vorticity, which is the summation of the inflow states λ as described in Ref. 22 and given by

$$\dot{\lambda} = F_1 \begin{Bmatrix} \ddot{\varepsilon} \\ \ddot{\beta} \end{Bmatrix} + F_2 \begin{Bmatrix} \dot{\varepsilon} \\ \dot{\beta} \end{Bmatrix} + F_3 \lambda = \begin{bmatrix} F_{1F} & F_{1B} \end{bmatrix} \begin{Bmatrix} \ddot{\varepsilon} \\ \ddot{\beta} \end{Bmatrix} + \begin{bmatrix} F_{2F} & F_{2B} \end{bmatrix} \begin{Bmatrix} \dot{\varepsilon} \\ \dot{\beta} \end{Bmatrix} + F_3 \lambda \tag{14}$$

To transfer the loads from the midchord (as defined above) to the wing reference axis, one may use

$$l_{ra} = l_{mc} \qquad m_{ra} = m_{mc} + dl_{mc} \qquad d_{ra} = d_{mc} \tag{15}$$

Furthermore, the loads are rotated to the body reference frame, which yields

$$F^{aero} = C^{Ba_1} \begin{Bmatrix} 0 \\ d_{ra} \\ l_{ra} \end{Bmatrix} \qquad M^{aero} = C^{Ba_1} \begin{Bmatrix} m_{ra} \\ 0 \\ 0 \end{Bmatrix} \tag{16}$$

where C^{Ba_1} is the transformation matrix from the local aerodynamic frame to the body frame. Note that the finite-span corrections are also included in the force distribution and may come from a CFD solution of the problem or experimental data if available. The aerodynamic loads about the midchord will be transferred to the wing elastic axis and rotated into the body frame for the solution of the equations of motion.

American Institute of Aeronautics and Astronautics

It is necessary to point out that the aerodynamic loads are applied by using the strip theory. Therefore, at each solution step (time step or pseudo-time step), it is necessary to find out velocity and inflow state distributions along the wing to determine the local angle of attack and the aerodynamics loads. Then the distributed aerodynamic loads can be transformed as the modal force (see Section G).

F. Equations of Motion with Rigid-Body Degrees of Freedom

For a beam with free rigid-body motions, one may need additional equations to describe the propagation of its body reference frame. This is particularly important in the coupled nonlinear aeroelastic and flight dynamic analysis. The complete system equations of motion are obtained by augmenting the equations of rigid-body motion and elastic deformations with the inflow equations, which can be represented as

$$\begin{bmatrix} M_{FF}(\varepsilon) & M_{FB}(\varepsilon) \\ M_{BF}(\varepsilon) & M_{BB}(\varepsilon) \end{bmatrix}\begin{Bmatrix} \ddot{\varepsilon} \\ \dot{\beta} \end{Bmatrix} + \begin{bmatrix} C_{FF}(\dot{\varepsilon},\varepsilon,\beta) & C_{FB}(\dot{\varepsilon},\varepsilon,\beta) \\ C_{BF}(\dot{\varepsilon},\varepsilon,\beta) & C_{BB}(\dot{\varepsilon},\varepsilon,\beta) \end{bmatrix}\begin{Bmatrix} \dot{\varepsilon} \\ \beta \end{Bmatrix} + \begin{bmatrix} K_{FF} & 0 \\ 0 & 0 \end{bmatrix}\begin{Bmatrix} \varepsilon \\ b \end{Bmatrix} = \begin{Bmatrix} R_F(\ddot{\varepsilon},\dot{\varepsilon},\varepsilon,\dot{\beta},\beta,\lambda,\zeta) \\ R_B(\ddot{\varepsilon},\dot{\varepsilon},\varepsilon,\dot{\beta},\beta,\lambda,\zeta) \end{Bmatrix}$$

$$\dot{\zeta} = -\frac{1}{2}\Omega_\zeta(\beta)\zeta \tag{17}$$

$$\dot{P}_B = \begin{bmatrix} C^{GB}(\zeta) & 0 \end{bmatrix}\beta$$

$$\dot{\lambda} = F_1\begin{Bmatrix} \ddot{\varepsilon} \\ \dot{\beta} \end{Bmatrix} + F_2\begin{Bmatrix} \dot{\varepsilon} \\ \beta \end{Bmatrix} + F_3\lambda$$

where ζ is the quaternions describing the orientation of the body frame B, P_B is the inertial position of the B frame, and C^{GB} is the rotation matrix from the body frame to the global frame G.[3]

G. Modal Solution of the Equations of Motion
The strain field along the beam coordinate s is approximated by the combination of linear normal modes

$$\varepsilon(s,t) = \Phi(s)\eta(t) \tag{18}$$

where Φ is the matrix of linear normal strain modes of the beam and η is the corresponding column matrix of the generalized modal coordiante. To obtain the normal modes in strain, one may first assume the modes in the classic displacement form, then derive the mode shapes in strain by taking additional spatial derivatives. This is only applicable for simple beam configurations. A more convenient approach is to use the strain-based finite-element equation (Eq. 10) and perform an eigenvalue analysis with the stiffness and inertia matrices. As the stiffness matrix in Eq. (10) is singular, one can find six zero eigenvalues, which correspond to the free-free rigid-body modes. The remaining eigenvalues are the frequencies for the coupled elastic and rigid-body modes. For the eigenvectors of these coupled modes, they generally take the following form

$$\Phi_C = \begin{Bmatrix} \Phi_F \\ \Phi_B \end{Bmatrix} \tag{19}$$

where Φ_F and Φ_B are the elastic and 6-by-1 rigid-body components of the modes, respectively. Since the modal approximation in Eq. (18) only requires the elastic deformation, the rigid-body component of these modes are removed, i.e.,

$$\Phi(s) = \Phi_F \tag{20}$$

After all, if a cantilever beam is to be solved, one only needs to take the elastic portion of the stiffness and inertial matrices (i.e., K_{FF} and M_{FF}) into the eigenvalue analysis, which yields the modes that satisfy the cantilever boundary condition. One more note about the normal modes is that they are not necessarily obtained about the undeformed shape. One can find normal modes about a geometrically nonlinear deformation. In doing so, the Jacobian matrix

from Eq. (11) should be evaluated about the nonlinear deformation, resulting in a different inertia matrix than the undeformed shape. However, the stiffness matrix remains the same.

After the normal modes are obtained, a modal transformation on the equations of motion (Eq. 17) can be performed based on Eq. (18), i.e.,

$$\bar{M}_{FF}\ddot{\eta} + \bar{M}_{FB}\dot{\beta} + \bar{C}_{FF}\dot{\eta} + \bar{C}_{FB}\beta + \bar{K}_{FF}\eta = \bar{R}_F(\eta,\dot{\eta},\ddot{\eta},\beta,\dot{\beta})$$

$$\bar{M}_{BF}\ddot{\eta} + \bar{M}_{BB}\dot{\beta} + \bar{C}_{BF}\dot{\eta} + \bar{C}_{BB}\beta = \bar{R}_B(\eta,\dot{\eta},\ddot{\eta},\beta,\dot{\beta})$$

$$\dot{\zeta} = -\frac{1}{2}\Omega_\zeta(\beta)\zeta \tag{21}$$

$$\dot{P}_B = \begin{bmatrix} C^{GB}(\zeta) & 0 \end{bmatrix}\beta$$

$$\dot{\lambda} = \begin{bmatrix} \bar{F}_{1F} & F_{1B} \end{bmatrix}\begin{Bmatrix} \ddot{\eta} \\ \dot{\beta} \end{Bmatrix} + \begin{bmatrix} \bar{F}_{2F} & F_{2B} \end{bmatrix}\begin{Bmatrix} \dot{\eta} \\ \beta \end{Bmatrix} + F_3\lambda$$

where

$$\bar{M}_{FF} = \Phi^T M_{FF}\Phi \qquad \bar{M}_{FB} = \Phi^T M_{FB} \qquad \bar{M}_{BF} = M_{BF}\Phi \qquad \bar{M}_{BB} = M_{BB}$$

$$\bar{C}_{FF} = \Phi^T C_{FF}\Phi \qquad \bar{C}_{FB} = \Phi^T C_{FB} \qquad \bar{C}_{BF} = C_{BF}\Phi \qquad \bar{C}_{BB} = C_{BB} \tag{22}$$

$$\bar{K}_{FF} = \Phi^T K_{FF}\Phi$$

$$\bar{F}_{1F} = F_{1F}\Phi \qquad \bar{F}_{2F} = F_{2F}\Phi$$

The load vector becomes

$$\begin{Bmatrix} \bar{R}_F \\ \bar{R}_B \end{Bmatrix} = \begin{Bmatrix} \Phi^T K_{FF}\Phi\eta^0 \\ 0 \end{Bmatrix} - \begin{bmatrix} \Phi^T J_{h\varepsilon}^T \\ J_{hb}^T \end{bmatrix}Ng + \begin{bmatrix} \Phi^T J_{p\varepsilon}^T \\ J_{pb}^T \end{bmatrix}B^F F^{dist} + \begin{bmatrix} \Phi^T J_{\theta\varepsilon}^T \\ J_{\theta b}^T \end{bmatrix}B^M M^{dist} + \begin{bmatrix} \Phi^T J_{p\varepsilon}^T \\ J_{pb}^T \end{bmatrix}F^{pt} + \begin{bmatrix} \Phi^T J_{\theta\varepsilon}^T \\ J_{\theta b}^T \end{bmatrix}M^{pt} \tag{23}$$

The modal solution is then peformed based on Eqs. (21) to (23).

III. Numerical Results

The strain-based geometrically nonlinear beam formulation has been implemented in the numerical framework UM/NAST: The University of Michigan's Nonlinear Aeroelastic Simulation Toolbox. Different solutions can be performed with the finite-element approach,[3-5, 12, 19, 20] including geometrically nonlinear static solution, nonlinear transient solution with forced excitations, linear modal solution, stability (flutter) analysis, etc. According to the formulation introduced in the previous section, the nonlinear static and transient solutions are implemented with the modal approach. Then, these two types of analyses will be carried out to study different geometrically nonlinear behavior of slender beams with different load conditions. In addition, some verification results are provided with respect to displacement-based MSC.Nastran solutions.[23]

A. Transient Solution of a Slender Cantilever Beam

Consider a slender cantilever isotropic beam (Fig. 3), whose geometric and physical properties are listed in Table 1. As shown, a sinusoidal vertical (dead) force is applied at the tip, given by

$$F(t) = \begin{cases} 0 & (t < 0) \\ A_F \sin\omega_F t & (t \geq 0) \end{cases} \tag{24}$$

with $A_F = 30$ N and $\omega_F = 20$ rad/s. The beam is solved in UM/NAST and MSC.Nastran with the beam discretized into 20 elements. The CBEAM element is selected in the MSC.Nastran model. For the modal solutions in UM/NAST, only the flatwise bending modes are considered, since the excitation is only in the vertical plane zx. The

flatwise bending modes and frequencies are obtained from the eigen problem defined by the finite-element approach. Table 2 summarizes the frequencies of the first five flatwise bending modes.
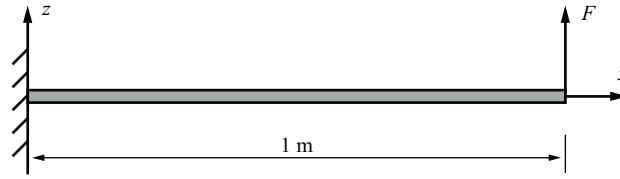

Figure 3. Cantilever beam with tip load.

Table 1.   Properties of a cantilever isotropic beam

Span (L)	1.00	m
Mass per span (m)	0.10	kg/m
Rotational moment of inertia	1.30×10^{-4}	kg·m
Flat bending moment of inertia	5.00×10^{-6}	kg·m
Edge bending moment of inertia	1.25×10^{-4}	kg·m
Extensional rigidity	1.00×10^{6}	N
Torsional rigidity	80.0	N·m^2
Flat bending rigidity	50.0	N·m^2
Edge bending rigidity	1.25×10^{3}	N·m^2

Table 2.   Natural modes and frequencies of the cantilever isotropic beam

No.	Mode	Frequency, Hz
1	1st flat bend	12.5
2	2nd flat bend	78.7
3	3rd flat bend	2.21×10^{2}
4	4th flat bend	4.37×10^{2}
5	5th flat bend	7.31×10^{2}

Figure 4 compares the normalized axial and vertical tip displacement results (as percentage of the beam span) from the different solutions. Basically, by selecting the first bending mode of the beam, one can recover (green line in the plot) the finite-element solutions from both MSC.Nastran and UM/NAST, except for the discrepancies at the peak values (1.4% relative difference). And this can be overcome by adding more modes in the solution. With two and three bending modes, the maximum relative errors are about 0.3% (black curve) and 0.1% (red curve), respectively. Figure 5 illustrates the profiles of the beam deformations from different solutions. One can only observe a very slight difference at the tip of the beam.

(a) Axial displacement   (b) Vertical displacement
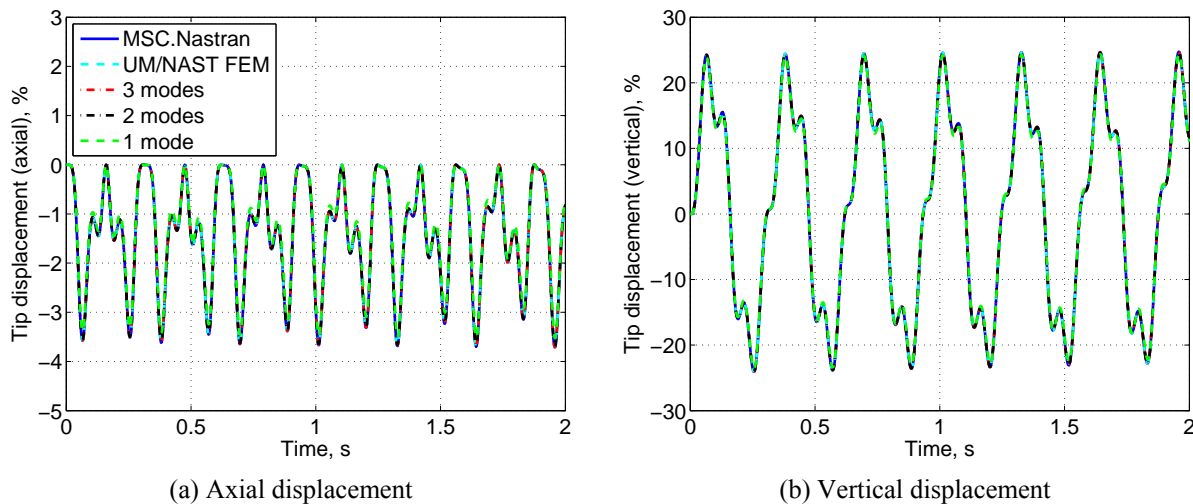
Figure 4. Tip displacement of the cantilever beam, normalized with respect to beam span.

10

American Institute of Aeronautics and Astronautics
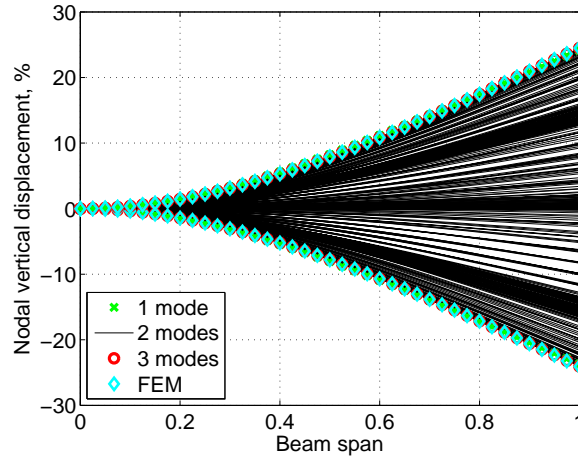
Figure 5. Profile of the deformation of the cantilever beam, normalized with respect to beam span.

Table 3 lists the problem size (in number of degrees of freedom) and CPU time of the four solutions, when solved on a PC with dual core at 2.26 GHz and 4 GB memory. It is evident that the complexity of the modal solutions is significantly reduced compared to the finite-element solution. In addition, modal solutions are more efficient than the finite-element solution, with over 24% reduction on CPU time. However, when varying the number of modes involved in the modal solutions, one cannot see prominent changes in the CPU time. This is due to the solution technique involved in the nonlinear modal strain-based solution. The generalized inertia and damping matrices and the force vector are nonlinear and dependent on the Jacoabians $J_{h\varepsilon}$, $J_{p\varepsilon}$, and $J_{\theta\varepsilon}$, which are updated at each time step with sub-iterations in the numerical integration based on the instantaneous strain vector (ε) converted from the modal coordinates (η). This means that the kinematic solution must be performed at each time step. It is a time-consuming process that compromises the efficiency gained by reducing the dimension of the problem.

Table 3.   Problem size and CPU time of different solutions for the cantilever beam

Solution	Dimension	CPU time, s
FEM	80	4.34×10^2
Modal: 1 mode	1	3.23×10^2
Modal: 2 modes	2	3.28×10^2
Modal: 3 modes	3	3.29×10^2
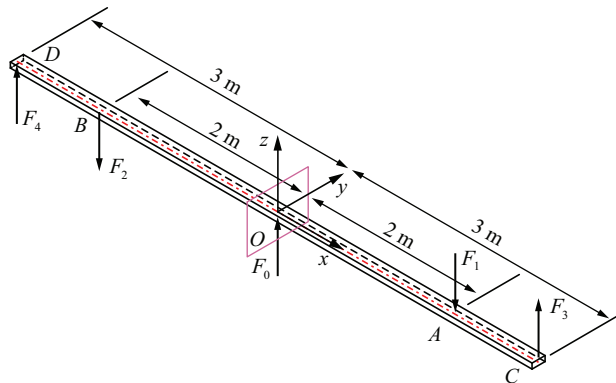
Figure 6. Flexible beam with multi-point excitations and free boundary condition.

B. Transient Response of a Slender Beam with Rigid-Body Motion (Free Boundary Condition)

The cantilever beam is now extended with a span of 6 m, while the cross-sectional properties are kept unchanged. There is no rigid-body constraint applied to the beam. Sinusoidal vertical forces governed by Eq. (24)

11
American Institute of Aeronautics and Astronautics

are applied at the locations indicated in Fig. 6, with the amplitudes of F_0 to F_4 being 44, -34, -34, 12, and 12 N, respectively. The frequencies of these excitations are all 5 Hz. The loads are so defined such that their summation at any time is zero. Transient response of the beam with such loading and boundary condition is obtained with both finite-element and modal approaches in UM/NAST, where the time step used is 0.0025 s.

The beam is first divided into 24 elements in UM/NAST to generate the modes with the rigid-body motions (Fig. 7). Note that there are six zero-frequency rigid-body modes associated with the beam, but they are not used in the modal solution. Even for the plots in Fig. 7, only the elastic components of the modes are shown and applied in the modal solution (Eq. 18). In addition, only the symmetric flatwise bending modes are considered due to the specific loading defined for the beam.
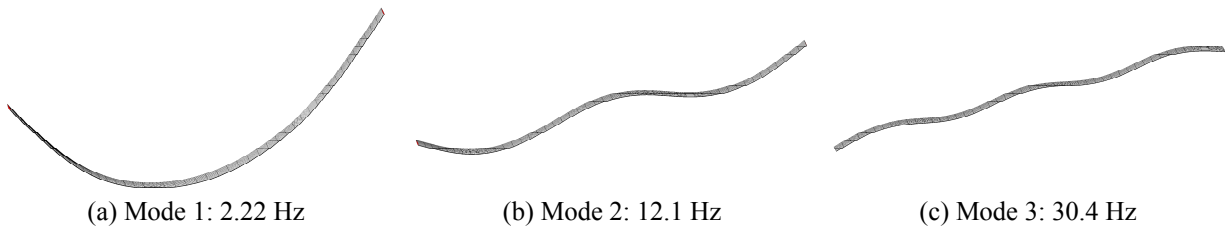
(a) Mode 1: 2.22 Hz   (b) Mode 2: 12.1 Hz   (c) Mode 3: 30.4 Hz
Figure 7. First three symmetric flatwise bending modes of the free flexible beam.

Figure 8 shows the vertical displacements at the stations at two thirds of the span (points A and B) and the tip (points C and D) of the beam. With the loads defined for the beam, nodal displacements lie in the vertical plane determined by the loads. Obviously, with only the first flatwise bending mode, it is not sufficient to accurately model the beam deformation. The loading is so applied to excite the second flatwise bending mode. Therefore, at least two modes are required to represent the beam motion. One may compare the modal solutions with 2 and 3 modes versus the finite-element results. The two-mode modal solution still deviates from the finite-element solution at some peak values, while the solution with three modes converges well to the finite-element solution. This can also be observed from the profile plot of the spanwise beam deformation (Fig. 9).
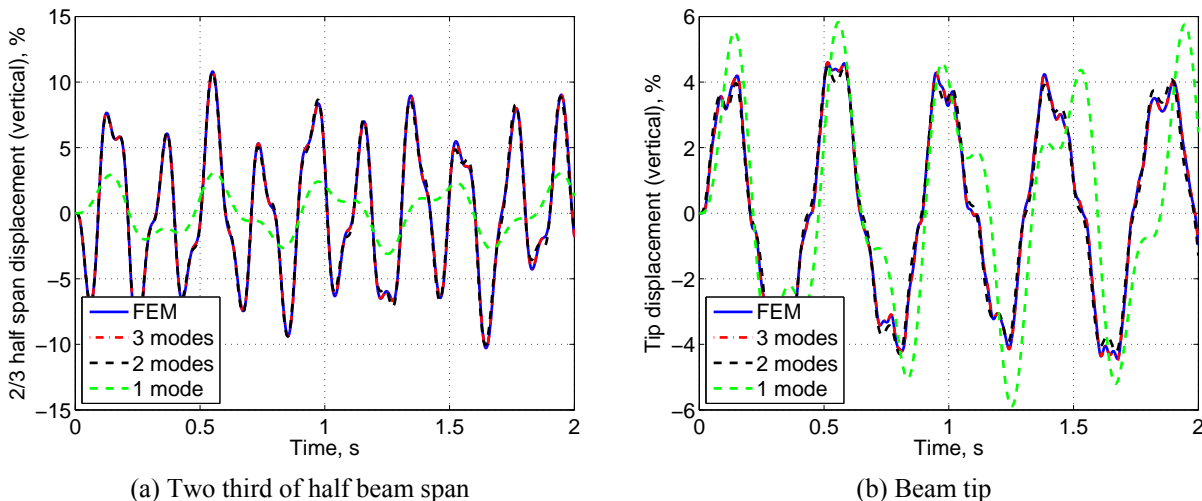
(a) Two third of half beam span   (b) Beam tip
Figure 8. Beam vertical displacements due to elastic deformation, normalized with respect to beam half span.

As there is no rigid-body constraint applied to the beam, it is also of interest to analyze its rigid-body motion. The middle point where a body reference frame is attached is selected to represent the rigid-body motion of the beam. Figure 10 plots the vertical displacement and velocity of that reference point. So the selection of the modes does impact the solution of the rigid-body motion.

Table 4 compares the problem size and CPU time of the different solutions for this flexible beam. The complexity of the problem to be solved is reduced in modal solutions. Again, due to the recovery of kinematics at each time step and sub-iterations within one time step, the time used for modal solutions (with two and three modes) is not significantly reduced compared to the finite-element method. The large reduction in the CPU time of the

modal solution with one mode is due to the fact that fewer sub-iterations are required to converge at each time steps than for the other cases.
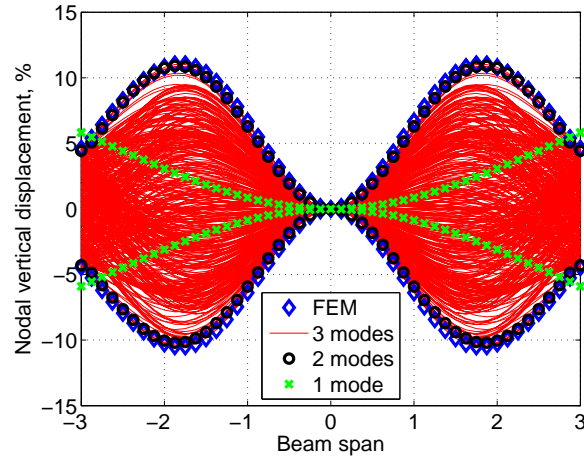

Figure 9. Beam elastic deformation profiles with different modes, normalized with respect to beam half span.
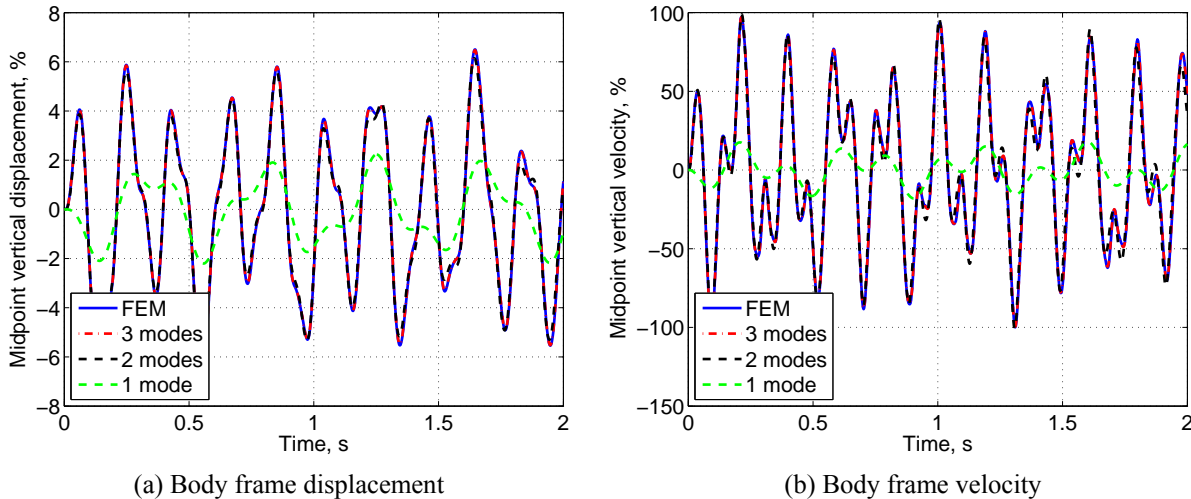

(a) Body frame displacement

(b) Body frame velocity

Figure 10.   Middle point (body frame) vertical displacement and velocity, displacement normalized with respect to beam half span, velocity normalized with respect to its max value (7.12 m/s).

Table 4.   Problem size and CPU time of different solutions for the free flexible beam

Solution	Dimension		CPU time, s
	Elastic	Rigid-body	
FEM	96	6	1.15×10^3
Modal: 1 mode	1	6	7.20×10^2
Modal: 2 modes	2	6	1.05×10^3
Modal: 3 modes	3	6	1.08×10^3

C. Description of a Highly Flexible Wing

In Ref. 1, a highly flexible, high-aspect-ratio wing was used for aeroelastic analyses. The physical and geometrical properties of the wing are given in Table 5. Natural frequencies and linear flutter speed of this model were calculated in Ref. 1. Natural modes are calculated for the undeformed beam using the finite element approach in the current formulation. The first few natural frequencies are listed in Table 6. An 8-element discretization was used in Ref. 1, whereas 10- and 20-element discretizations are employed in the current work for convergence studies. These results are all compared with analytical solutions. As can be observed, the current formulation gives

American Institute of Aeronautics and Astronautics

accurate numerical predictions on the fundamental frequencies of the slender beam, when compared to the analytical solutions.

Table 5.   Properties of a highly flexible wing (after Ref. 1)

Span (L)	16	m
Chord (c)	1	m
Beam ref. axis (from l.e.)	50%	chord
Cross-sectional $c.g.$ (from l.e.)	50%	chord
Mass per span (m)	0.75	kg/m
Rotational moment of inertia	0.1	kg·m
Torsional rigidity	1.00×10^4	N·m^2
Flat bending rigidity	2.00×10^4	N·m^2
Edge bending rigidity	4.00×10^6	N·m^2

Table 6.   Natural modes and frequencies of the highly flexible wing (Hz), about its undeformed shape

No.	Mode	Ref. 1	Strain-based beam (10 elements)	Strain-based beam (20 elements)	Analytical solution
1	1st flat bend	0.358	0.358	0.357	0.357
2	2nd flat bend	2.33	2.27	2.25	2.24
3	1st torsion	4.96	4.95	4.94	4.94
4	1st edge bend	5.05	5.06	5.05	5.05
5	3rd flat bend	7.01	6.53	6.33	6.26
6	4th flat bend	--	13.3	12.5	12.3
7	2nd torsion	--	15.0	14.9	14.8
8	5th flat bend	--	23.2	21.0	20.3
9	3rd torsion	--	25.3	24.9	24.7
10	2nd edge bend	--	32.2	31.8	31.6

Using the strain-based formulation, the linear flutter result, at the 20,000 m altitude without gravity effects, is obtained and compared with what was presented in Ref. 1 (see Table 7). The current strain-based formulation predicts identical linear results as Ref. 1. In addition, the nonlinear flutter boundary (root pitch angle = 2°) is also calculated with this cantilever wing (see Table 7). The flutter mode is a coupled second flatwise bending and first torsion, while the in-plane bending component in the flutter mode is not significant (see Fig. 11). Note that the flutter boundaries are obtained using the approach introduced in Ref. 4, where the finite-element solution of the system equations were involved. In the coming sections, simulations are performed to study the static deformation and post-flutter behavior of the flexible cantilever wing by using the modal analysis.

Table 7.   Flutter boundary of the highly flexible wing

	Ref. 1	Current (linear)	Current (nonlinear)
Velocity (m/s)	32.2	32.2	23.3
Frequency (Hz)	3.60	3.60	1.61
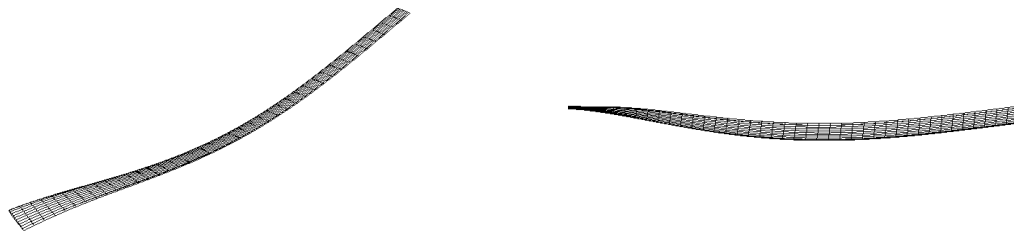
Figure 11.   Flutter mode of the flexible wing (left: angle view; right: font view).

14
American Institute of Aeronautics and Astronautics

D. Static Aeroelastic Solution of the Highly Flexible Wing

To assess the convergence of the static modal solutions for the aeroelastic problem, a series of calculations are performed to obtain the static deformations of the flexible wing with different numbers of modes. The freestream velocity is 25 m/s (greater than its nonlinear flutter boundary) and the root pitch angle is 2° (the same as the one used for the nonlinear flutter calculation). Figures 12 to 14 exemplify the convergence trend when more modes are involved in the calculation, where the black lines in the plots represent the result of the finite-element solution with 20 elements (the reference solution). In the modal solutions, the modes are selected from the list in Table 6 with 20-element discretization. As one can observe from the plots, the modal solution including the first three modes is sufficiently accurate since the relative errors of the tip displacements in the three directions are all less than 2%. A more accurate solution can be obtained with seven modes included, where the relative error of the tip displacements is within 0.5%.
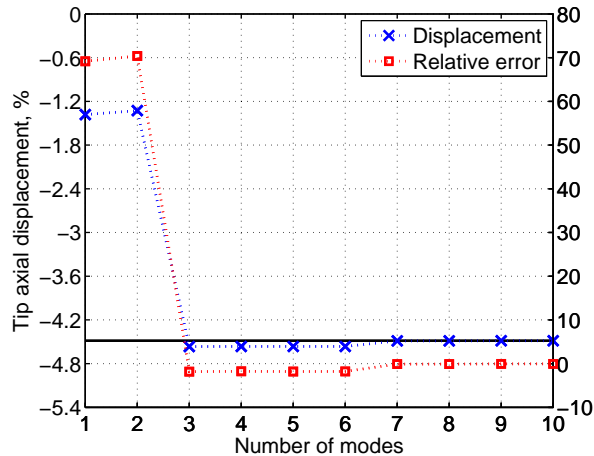
Figure 12.   Change of the steady state tip displacement (axial) with number of modes, using modes about the undeformed shape.
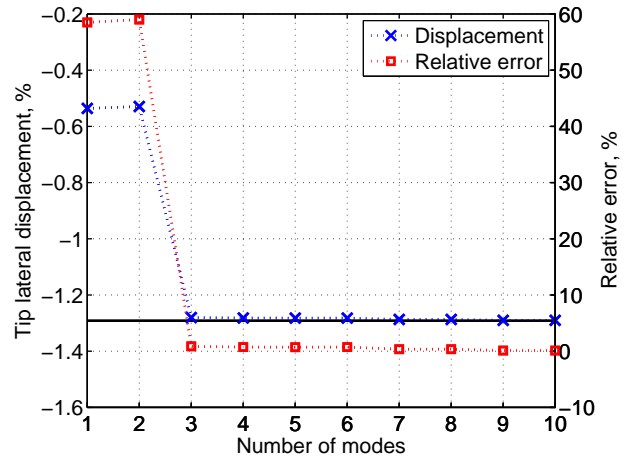
Figure 13.   Change of the steady state tip displacement (lateral) with number of modes, using modes about the undeformed shape.
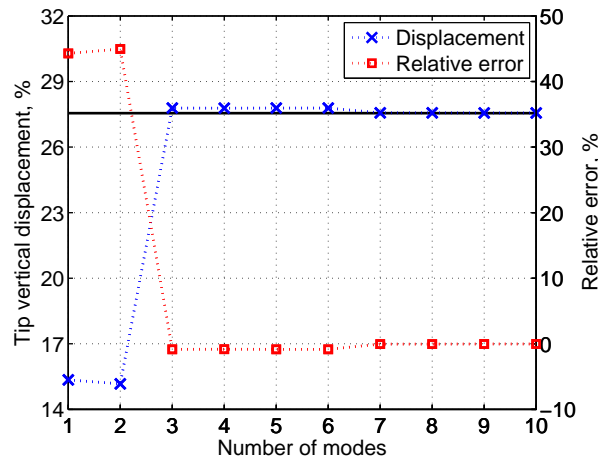
Figure 14.   Change of the steady state tip displacement (vertical) with number of modes, using modes about the undeformed shape.

Another set of static modal solutions is conducted using the modeshapes about a beam deformed shape. Particularly, the deformation under loads generated from a 25 m/s freestream velocity is obtained (using FEM), about which another set of modeshapes is obtained (see Appendix for the plots of these modes). Based on this new set of modes, the static deformation could be approximated again and compared to the finite-element results. From these, one finds the convergence of the solution using modes about the deformed shape is faster than the one using the undeformed shape. To reach the same 0.5% relative error, only five modes are required in the solution (see Figs. 15 to 17).
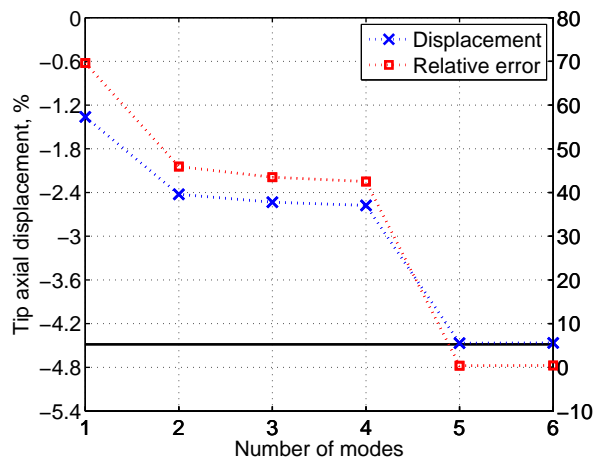
Figure 15.   Change of the steady state tip displacement (axial) with number of modes, using modes about the deformed state with 25 m/s freestream velocity.
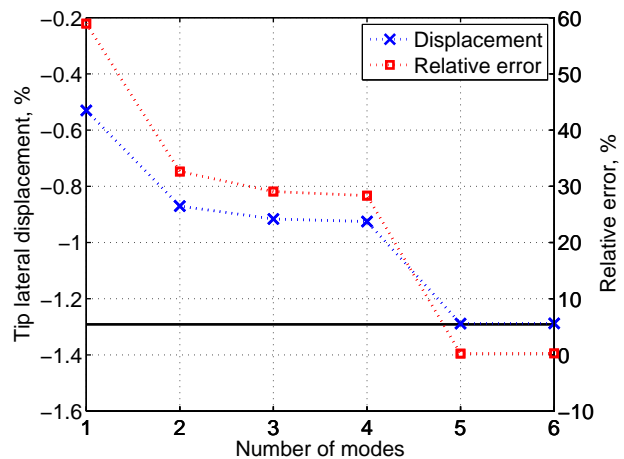

Figure 16.   Change of the steady state tip displacement (lateral) with number of modes, using modes about the deformed state with 25 m/s freestream velocity.
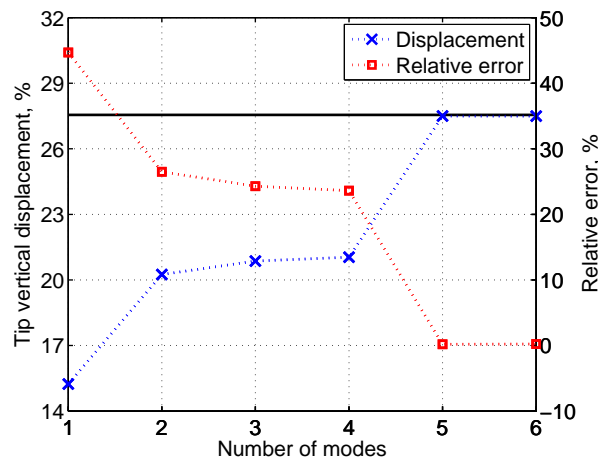

Figure 17.   Change of the steady state tip displacement (vertical) with number of modes, using modes about the deformed state with 25 m/s freestream velocity.

E. Limit-Cycle Oscillation of the Highly Flexible Wing

In this section, transient response of the highly flexible wing is analyzed. The wing is first brought to its nonlinear static deformation with the freestream velocity of 25 m/s, calculated in the previous section. The deformed shape serves as the initial condition for the transient simulations. Both finite-element (20 elements) and modal simulation cases (see Table 8) are solved. Note that the modes used for the modal solutions are selected from the list of Table 6, which are obtained about the undeformed state. As the freestream velocity is higher than the flutter boundary (23.3 m/s), the wing is expected to self-excite. The amplitude of the wing oscillation would increase, until it reaches the limit-cycle oscillation (LCO).

Table 8.   Transient analysis cases of the highly flexible wing with normal modes about the undeformed shape

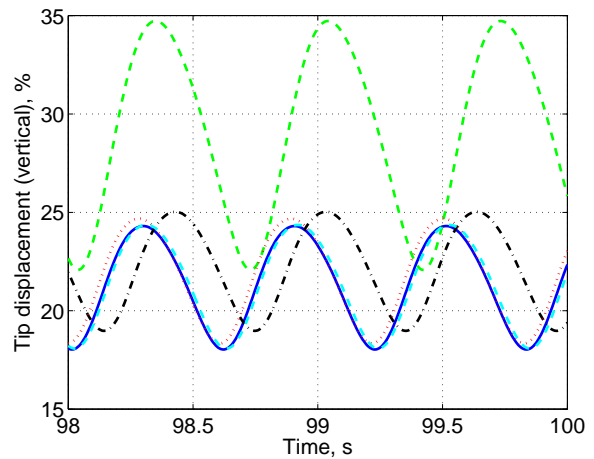| Case	1	2	3	4	5
Description	FEM	Modes 1 - 4	Modes 1 - 7	Modes 1 - 9	Modes 1 - 15
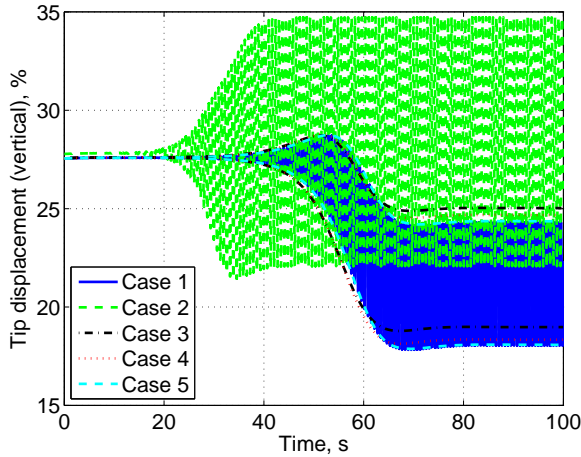
(a) Time: 0-100 s (contours of Cases 3 to 5 are provided)
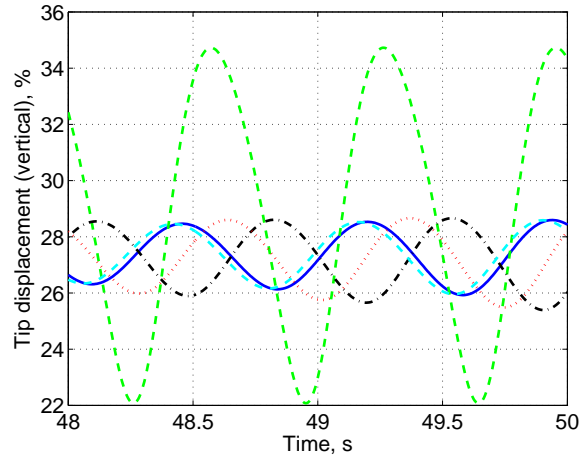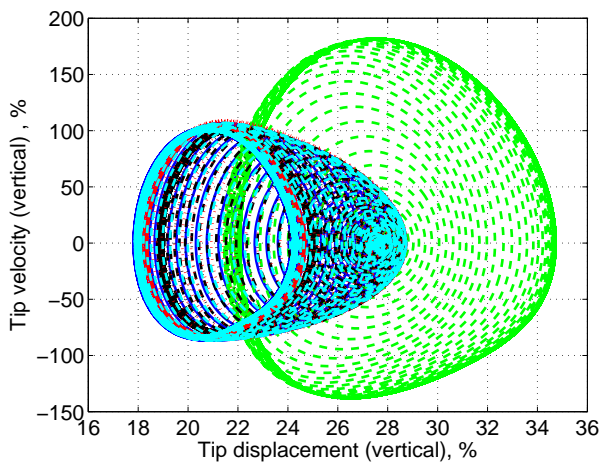
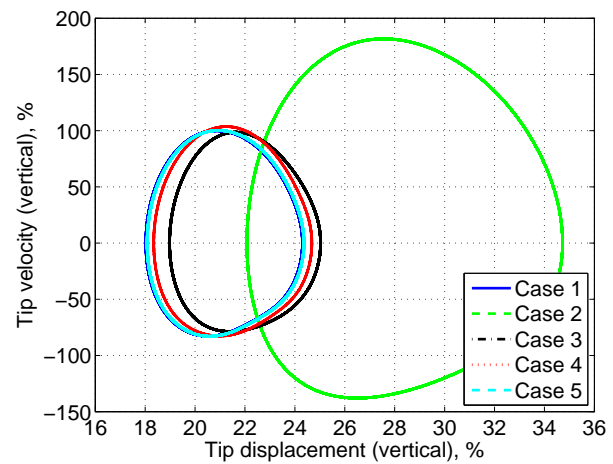(b) Time: 48-50 s
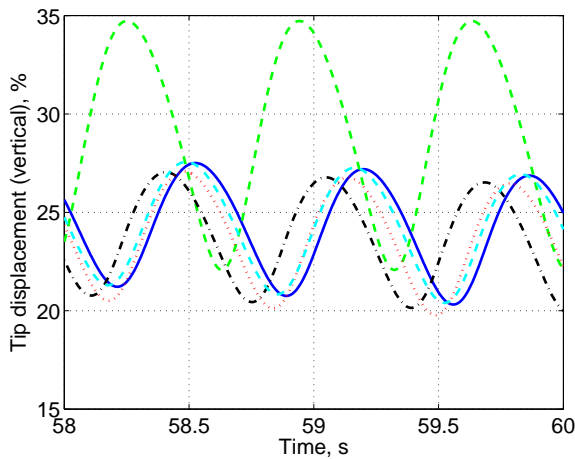
(c) Time: 58-60 s

(d) Time: 98-100 s

Figure 18.   LCO of the highly flexible wing, solution with normal modes about the undeformed shape.

(a) Time: 0-100 s

(b) Time: 85-100 s

Figure 19.   Phase-plane plot of the wing tip motion, displacement normalized by wing span, velocity normalized by the maximum value from the FEM solution (6.27 m/s).

Figure 18a shows the time history (from 0 to 100 s) of the tip vertical displacement. Note that the quantities are normalized by the wing span. For clarity purpose, profile contours for Cases 3 to 5 are provided in this plot, such that the reference finite-element results can be clearly observed. Figures 18b and 18c give the transient response when the LCO is still developing, while Fig. 18d exemplifies the steady state of the LCO. A phase-plane plot of the wing tip motion is provided in Fig. 19. In addition, one can take the 20 periods of the wing tip displacement after 85 s, when the LCO is set, and perform an FFT to obtain the frequency components of the response, which is plotted in Fig. 20. From Figs. 19 and 20, one can basically see a one-frequency LCO of this aeroelastic system.

As shown in the figures, with the selection of the first four modes (Case 2, green curve), it is possible to predict the instability of the aeroelastic system. The transient response eventually develops into an LCO. However, its magnitude (Fig. 18), phase (Fig. 19), and frequency (Fig. 20) do not agree with the reference finite-element simulation at all, which predits a completely different LCO behavior. Note that it was already sufficient to use only the first four modes to provide converged static solutions (see Figs. 12 to 14). Therefore, it is necessary to include more modes in the transient analysis to converge the solution. That is how the study is performed in this work, as Cases 3 to 5 are carried out with 7, 9, and 15 modes, respectively. Obviously, the convergence gets better with more modes involved and with 15 modes, the modal analysis results agree with those from the finite-element analysis. From this analysis, it is evident to conclude that one needs to use more modes in modal transient analysis than the static solution as expected, for this aeroelastic problem.
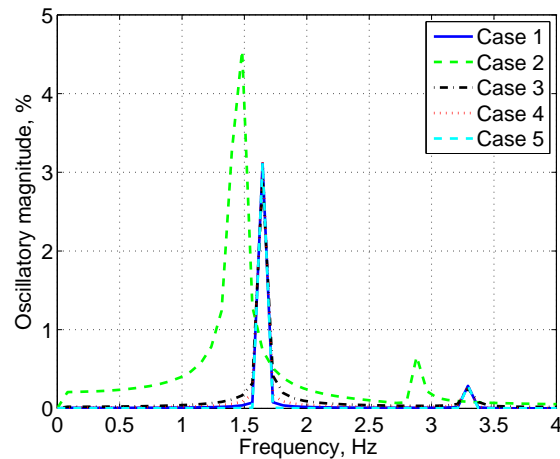

Figure 20.   FFT of the tip oscillation of the highly flexible wing (20 periods after 85 s), amplitude normalized by wing span.

Table 9 still compares the problem size and the CPU time for the different solutions of the aeroelastic problem. In the simulations, the wing is divided into 20 stations, on which the inflow velocity is calculated with the expansion of 6 inflow states. Therefore, the total number of aerodynamic states is 120. The current study does not vary the number of strips in the aerodynamic calculation. Further parametric study can be performed to evaluate the impact of different number of aerodynamic strips and states in the aeroelastic solution. Form the comparison of CPU time, one can see that the modal solutions are taking longer than the direct FEM one. This is due to the fact that nodal orientations are recovered in the intermediate steps of the time integrations, in addition to the Jacobians required in the simulations with only structural loads. The nodal orientations are used to determine the local aerodynamic frames (by using C^{Ba1}), such that the velocity components and angles of attack are obtained.

Table 9.   Problem size and CPU time of different transient solutions of the highly flexible wing with normal modes about the undeformed shape

Solution	Dimension		CPU time, s
	Elastic	Aerodynamic	
Case 1	80	120	3.09×10^4
Case 2	4	120	3.29×10^4
Case 3	7	120	3.35×10^4
Case 4	9	120	3.40×10^4
Case 5	15	120	3.56×10^4

American Institute of Aeronautics and Astronautics

Similar to the static analysis, the normal modes about the deformed shape can also be used as the reference modes in the transient analysis. Now the normal modes are determined about the beam deformed shape under 25 m/s freestream. Different modal analysis cases are compared to the finite-element solution (see Table 10). Again the time history of the wing tip vertical displacement, the phase-plane plot of the wing tip motion, and the FFT results of the wing tip displacement are plotted in Figs. 21 to 23, respectively.

Table 10. Transient analysis cases of the highly flexible wing with normal modes about the deformed shape

Case	1	2	3	4	5
Description	FEM	Modes 1 - 4	Modes 1 - 5	Modes 1 - 7	Modes 1 - 9

(a) Time: 0-100 s (contours of Cases 3 to 5 are provided)

(b) Time: 48-50 s

(c) Time: 58-60 s

(d) Time: 98-100 s
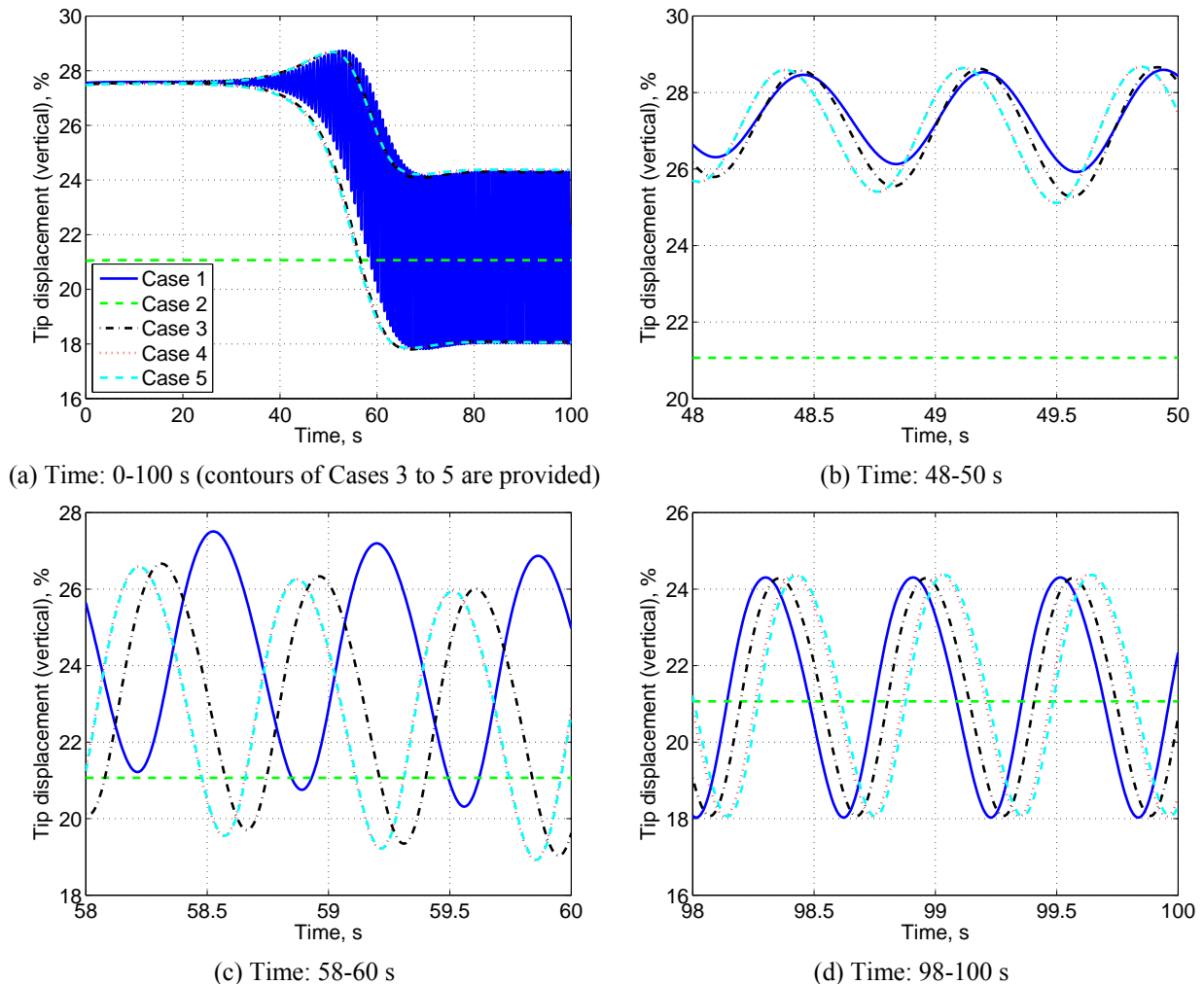
Figure 21. LCO of the highly flexible wing, solution with normal modes about the deformed shape.

Figure 21a plots the time history of the vertical displacement for the wing tip. Profile contours for Cases 3 to 5 are provided in this plot, such that the reference finite-element results can be clearly observed. Different stages in the time history are also illustrated in Figure 21b to 21d. It can be observed that with only four modes (Case 2, green curve), the simulation starts from a different initial (static) condition and does not predict instability at all. A minimum of five modes is required to capture the instability of the system. Figure 22 exemplifies the motion of wing tip with the phase-plane plot. One can clearly see that Case 2 behaves differently from all the other cases, which reduces to a point in the phase-plane plot and no oscillation is observed. From Figs. 21b, 21c, and 22a, the phase difference of the other cases can be observed at the transient stages of the simulations, when the limit-cycle oscillation is still developing. However, after the LCO is set up (Figs. 21d, and 22b), the phase difference is reduced

American Institute of Aeronautics and Astronautics

and maintains constant. In addition, the magnitude of the oscillations (displacement and velocity) from the modal solutions (Cases 3 to 5) is very close to what the finite-element solution predicts. From the plot of Fig. 23, the frequency components of the responses in Cases 3 to 5 are almost the same as the finite-element solution. Therefore, the solution with five modes (Case 3, black curve) is already good enough compared to the finite-element result. It has some phase difference from the FEM results, but the magnitude and frequency match well. With more modes included, the convergence quality is slightly, but not significantly, improved. Overall, the simulations using the modes about the deformed shape converge faster compared to the simulations using the normal modes about the undeformed shape. Note that, selection of the first five modes about the deformed shape also gave nicely converged static solutions.

| (a) Time: 0-100 s | (b) Time: 85-100 s |
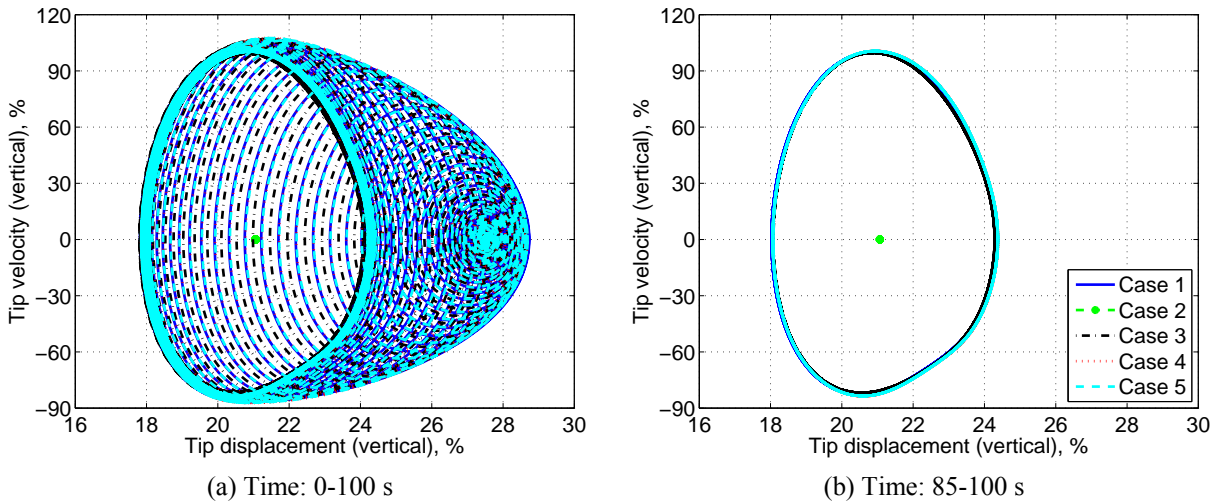
Figure 22. **Phase-plane plot of the wing tip motion, displacement normalized by wing span, velocity normalized by the maximum value from the FEM solution (6.27 m/s).**
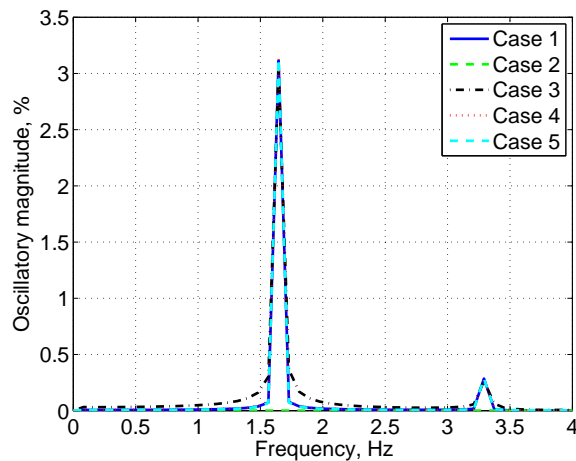

Figure 23. **FFT of the tip displacement of the highly flexible wing (20 periods after 85 s), amplitude normalized by wing span.**

IV. Concluding Remarks

This paper discussed a modal solution to the strain-based geometrically nonlinear beam formulation. The original strain-based geometrically nonlinear beam formulation is able to capture the arbitrarily large deformations of slender structures. The theory defines beam extension strain and bending/twist curvatures as independent states, which makes no approximation to the deformation of beam reference line. Therefore, this formulation is geometrically exact and can accurately model the composite beam deformation. The strain-based formulation

features fewer degrees of freedom than the displacement-based and the mix-form formulations to represent the same deformation complexity. In addition, this formulation solves directly for the beam curvatures that are the variables measured by typical sensors in control studies (e.g., strain gages).

The linear normal modes in strain are used to approximate the strain distribution (also displacement distribution through the recovery of kinematics) along the beam. With this modal approximation, the size of the problem is further reduced, compared to the full finite-element form. This reduction in problem size did save the computational cost in some transient analyses, but in general was different from the full FEM. Another advantage of the strain-based modal solution is its simplicity to find the geometrically nonlinear static solution. With a few modes involved, one can find out the accurate static solution. Moreover, the generalized modal stiffness matrix is constant, which means it does not need to be updated over the iterations to find the converged nonlinear static state. This makes this solution approach very suitable for the trim solution of very flexible aircraft, where the solution is fundamentally static with large deformations.

Nonlinear transient analyses were also performed for various beams with structural or aerodynamic loads. Of more interests are the simulations of limit-cycle oscillation for a highly flexible cantilever wing. From the numerical study, it is concluded that the use of normal modes about the geometrically nonlinear deformed shape may improve the convergence of the solution, in that fewer modes are required to reach the converged solution. This is also of importance in the nonlinear aeroelastic analysis of very flexible aircraft. One needs to determine the geometrically nonlinear trim state, about which the linearization is performed to get the normal modes. Transient analysis may be performed by properly selecting these modes.

As can be observed from the numerical studies, the computational advantage of the modal solution was sacrificed due to the requirement of recovering wing displacement and rotation at the intermediate steps in the time integration. Additional study is required to find a better way to handle the intermediate wing displacement/rotation in the time integrations to improve the computational efficiency of the modal approach.

Appendix

Listed here are the first ten modes obtained for the cantilever wing about its deformed shape as the result of aerodynamic loading generated from a 25 m/s freestream flow.
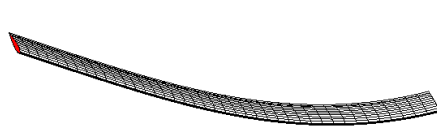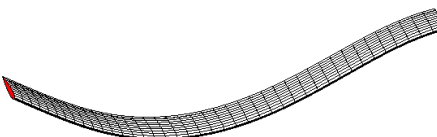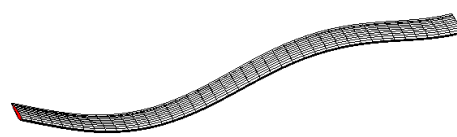

MODE 1: 0.358 Hz

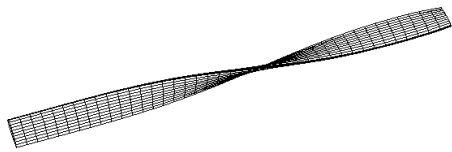**Figure A1. First mode.**

MODE 2: 1.49 Hz

Figure A2. Second mode.

MODE 3: 2.22 Hz

Figure A3. Third mode.

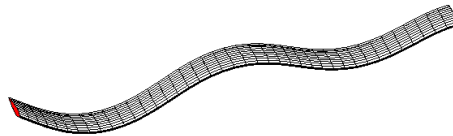MODE 4: 6.2 Hz

Figure A4. Fourth mode.

American Institute of Aeronautics and Astronautics
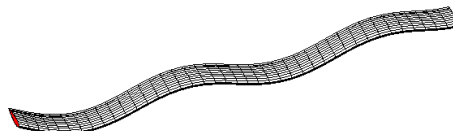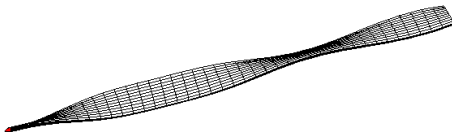
MODE 5: 6.94 Hz

Figure A5. Fifth mode.

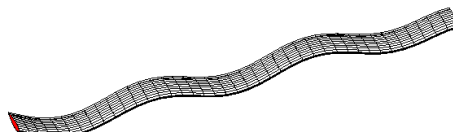MODE 6: 12.4 Hz

Figure A6. Sixth mode.
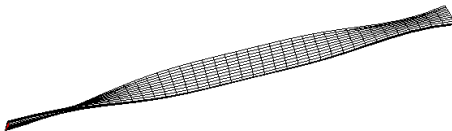
MODE 7: 17.4 Hz

Figure A7. Seventh mode.

MODE 8: 20.8 Hz

Figure A8. Eighth mode.

MODE 9: 28.8 Hz

Figure A9. Ninth mode.

MODE 10: 31.6 Hz

Figure A10. Tenth mode.

References

[1]Patil, M. J., Hodges, D. H. and Cesnik, C. E. S., "Nonlinear Aeroelasticity and Flight Dynamics of High-Altitude Long-Endurance Aircraft," *Journal of Aircraft*, Vol. 38, No. 1, 2001, pp. 88-94.

[2]Livne, E. and Weisshaar, T. A., "Aeroelasticity of Nonconventional Airplane Configurations - Past and Future," *Journal of Aircraft*, Vol. 40, No. 6, 2003, pp. 1047-1065.

[3]Shearer, C. M. and Cesnik, C. E. S., "Nonlinear Flight Dynamics of Very Flexible Aircraft," *Journal of Aircraft*, Vol. 44, No. 5, 2007, pp. 1528-1545.

[4]Su, W. and Cesnik, C. E. S., "Nonlinear Aeroelasticity of a Very Flexible Blended-Wing-Body Aircraft," *Journal of Aircraft*, Vol. 47, No. 5, 2010, pp. 1539-1553.

[5]Su, W. and Cesnik, C. E. S., "Dynamic Response of Highly Flexible Flying Wings," *AIAA Journal*, Vol. 49, No. 2, 2011, pp. 324-339.

[6]Bauchau, O. A. and Hong, C. H., "Nonlinear Composite Beam Theory," *Journal of Applied Mechanics - Transactions of the ASME*, Vol. 55, No. 1, 1988, pp. 156-163.

[7]Hodges, D. H., "A Mixed Variational Formulation Based on Exact Intrinsic Equations for Dynamics of Moving Beams," *International Journal of Solids and Structures*, Vol. 26, No. 11, 1990, pp. 1253-1273.

[8]Palacios, R. and Cesnik, C. E. S., "Geometrically Nonlinear Theory of Composite Beams with Deformable Cross Sections," *AIAA Journal*, Vol. 46, No. 2, 2008, pp. 439-450.

[9]Hodges, D. H., "Geometrically Exact, Intrinsic Theory for Dynamics of Curved and Twisted Anisotropic Beams," *AIAA Journal*, Vol. 41, No. 6, 2003, pp. 1131-1137.

[10]Zupan, D. and Saje, M., "Finite-Element Formulation of Geometrically Exact Three-Dimensional Beam Theories Based on Interpolation of Strain Measures," *Computer Methods in Applied Mechanics and Engineering*, Vol. 192, No. 49-50, 2003, pp. 5209-5248.

[11]Gams, M., Planinc, I. and Saje, M., "The Strain-Based Beam Finite Elements in Multibody Dynamics," *Journal of Sound and Vibration*, Vol. 305, No. 1-2, 2007, pp. 194-210.

[12]Su, W. and Cesnik, C. E. S., "Strain-Based Geometrically Nonlinear Beam Formulation for Modeling Very Flexible Aircraft," *International Journal of Solids and Structures*, Vol. 48, No. 16-17, 2011, pp. 2349-2360.

[13]Palacios, R., Murua, J. and Cook, R., "Structural and Aerodynamic Models in Nonlinear Flight Dynamics of Very Flexible Aircraft," *AIAA Journal*, Vol. 48, No. 11, 2010, pp. 2648-2659.

[14]Tang, D. and Dowell, E. H., "Experimental and Theoretical Study on Aeroelastic Response of High-Aspect-Ratio Wings," *AIAA Journal*, Vol. 39, No. 8, 2001, pp. 1430-1441.

[15]Tang, D. and Dowell, E. H., "Experimental and Theoretical Study of Gust Response for High-Aspect-Ratio Wing," *AIAA Journal*, Vol. 40, No. 3, 2002, pp. 419-429.

[16]Tang, D. and Dowell, E. H., "Limit-Cycle Hysteresis Response for a High-Aspect-Ratio Wing Model," *Journal of Aircraft*, Vol. 39, No. 5, 2002, pp. 885-888.

[17]Patil, M. J. and Althoff, M., "Energy-Consistent, Galerkin Approach for the Nonlinear Dynamics of Beams Using Mixed, Intrinsic Equations," AIAA-2006-1737, *47th AIAA / ASME / ASCE / AHS / ASC Structures, Structural Dynamics, and Materials Conference*, Newport, Rhode Island, May 1-4 2006.

[18]Palacios, R., "Nonlinear Normal Modes in an Intrinsic Theory of Anisotropic Beams," *Journal of Sound and Vibration*, Vol. 330, No. 8, 2011, pp. 1772-1792.

[19]Cesnik, C. E. S. and Brown, E. L., "Modeling of High Aspect Ratio Active Flexible Wings for Roll Control," AIAA-2002-1719, *43rd AIAA / ASME / ASCE / AHS / ASC Structures, Structural Dynamics, and Materials Conference*, Denver, Colorado, Apr. 22-25, 2002.

[20]Cesnik, C. E. S. and Su, W., "Nonlinear Aeroelastic Modeling and Analysis of Fully Flexible Aircraft," AIAA-2005-2169, *46th AIAA / ASME / ASCE / AHS / ASC Structures, Structural Dynamics, and Materials Conference*, Austin, Texas, Apr. 18-21, 2005.

[21]Palacios, R. and Cesnik, C. E. S., "Cross-Sectional Analysis of Nonhomogeneous Anisotropic Active Slender Structures," *AIAA Journal*, Vol. 43, No. 12, 2005, pp. 2624-2638.

[22]Peters, D. A. and Johnson, M. J., "Finite-State Airloads for Deformable Airfoils on Fixed and Rotating Wings," *Proceedings of Symposium on Aeroelasticity and Fluid Structure Interaction Problems, ASME Winter Annual Meeting*, edited by P. P. Friedmann and J. C. I. Chang, AD - Vol. 44, The American Society of Mechanical Engineers, New York, New York, 1994, pp. 1-28.

[23]MSC.Software, *MSC.Nastran 2004 Quick reference Guide - Volume 1*, MSC.Software Corporation, Santa Ana, California, 2003.